LA-UR-18-23434
Approved for public release; distribution is unlimited.

Title: Beam dynamics modeling of the proton RFQ MEBT with CST Particle Studio

Author(s): Kurennoy, Sergey S.

Intended for: External distribution

Issued: 2018-04-20

Los Alamos
NATIONAL LABORATORY

Technical Note

Accelerator Operation and Technology
AOT-AE Group:
Accelerators & Electrodynamics

To/MS: Distribution
From/MS: Sergey Kurennoy, AOT-AE / H817
Phone/Fax: 505-665-1459 / 505-667-2807
E-mail: kurennoy@lanl.gov

Symbol: AOT-AE: 18-005 (TN)
Date: April 10, 2018

SUBJECT: Beam dynamics modeling of the proton RFQ MEBT with CST Particle Studio

Beam dynamics in the Medium-Energy Beam Transfer (MEBT) after the new proton RFQ for the LANSCE injector is modeled with the CST Particle Studio PIC solver. The modeling uses the CST-calculated 3D EM fields of MEBT elements, which is important because (i) the beam size in MEBT is large, comparable to the beam-pipe aperture, and (ii) the fields of neighboring MEBT elements overlap. Our results indicate significant beam emittance growth not predicted by traditional beam dynamics codes.

Distribution:

AOT-AE			(e-mail copy)
R.W. Garnett	AOT-DO	MS H809	(e-mail copy)
S.V. Milton	AOT-DO	MS H809	(e-mail copy)
J.L. Medina	AOT-MDE	MS H838	(e-mail copy)
J.P. Montross	AOT-MDE	MS H838	(e-mail copy)
J.F. O'Hara	AOT-MDE	MS H838	(e-mail copy)
R. Bratton	AOT-RFE	MS H827	(e-mail copy)
J.T.M. Lyles	AOT-RFE	MS H827	(e-mail copy)
D.E. Rees	AOT-RFE	MS H827	(e-mail copy)

1. Introduction.

A modern front end for the LANSCE linac is under development [1]. The aging Cockcroft-Walton based injectors will be replaced by modern RFQ-based ones. Two lines, one for H^+ (proton) and the other for H^- ions, will produce 750-keV beams that merge into a common transport, which goes to the entrance of the first DTL tank. Both injector lines will include an RFQ, buncher cavities, and focusing quadrupoles. However, the line designs for positive and negative ions are quite different because the H^- line has to incorporate the beam chopper. The existing common transport line for different beam species creates significant constrains for the injector line design. The first challenge is a very long distance from the proton RFQ exit to the DTL entrance, more than 4 m. Second, because the two beam lines merge at 18-degree angle, the horizontal space for proton-line elements is limited by the existing hardware near the merging area, as illustrated in Fig. 1. Therefore, a specialized medium-energy beam transfer (MEBT) after the new proton RFQ at 750 keV was developed [2] with envelope codes, and the beam dynamics in MEBT was modeled using Parmila. The proton MEBT includes two compact quarter-wave RF bunchers and four short quadrupoles with steerers, all within the length of about 1 m. Figure 1 (courtesy of Ray Roybal and Jason Medina) shows a draft engineering model of the proton RFQ injector (elements with red labels) near its merging with the existing H^- transfer line (blue labels, only elements near the merging point are shown) at the common bending dipole. The green structures in Fig. 1 are the existing support structures.

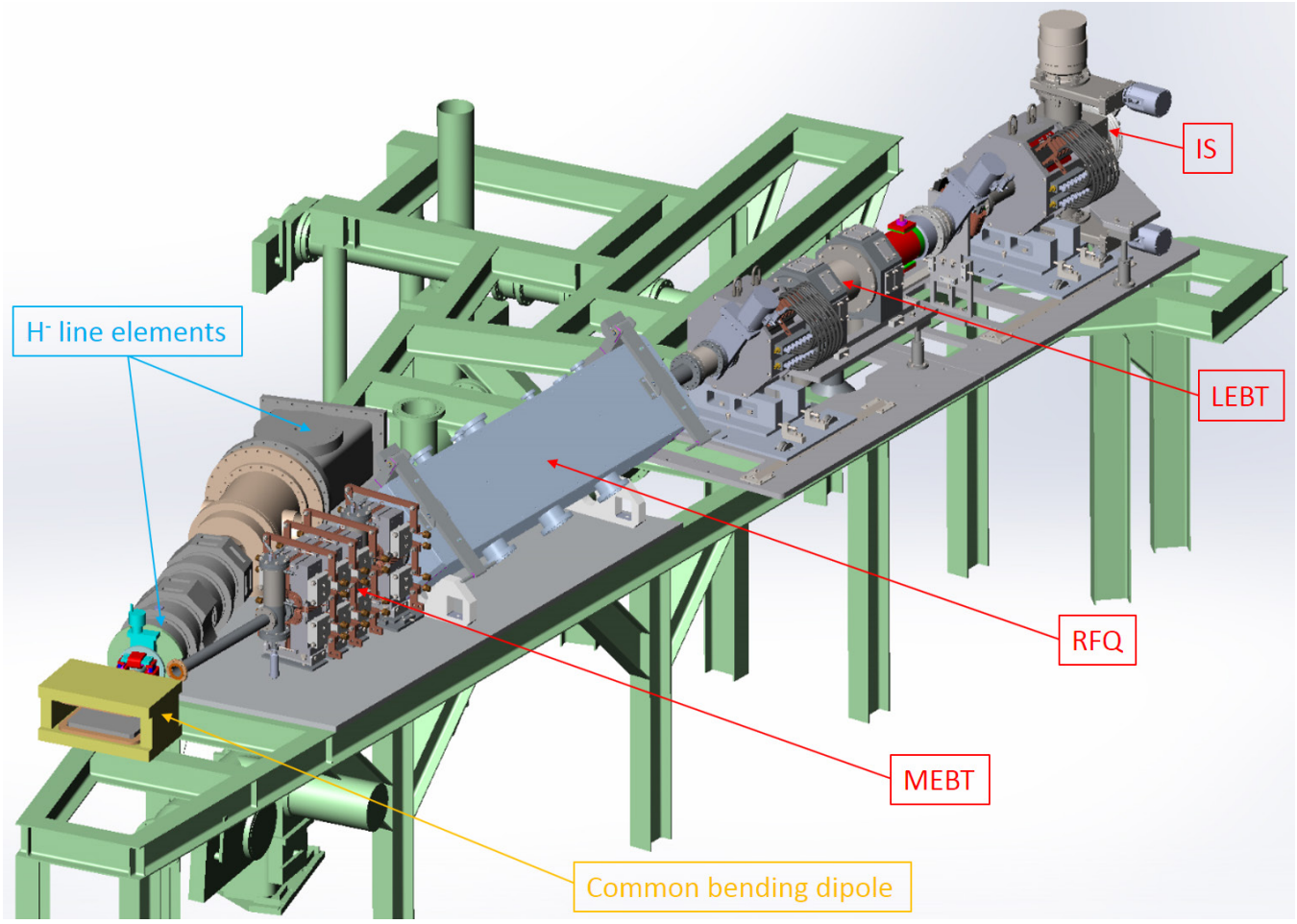

Figure 1: Proton RFQ injector engineering model in the LANSCE injector area.

The proton beam size in the MEBT is large, comparable to the beam-pipe aperture, hence one can expect that non-linear 3D field effects at large radii become important. Using CST Studio codes [3], we calculated buncher RF fields and quadrupole magnetic fields in [4]. Here we use the calculated 3D fields to perform particle-in-cell (PIC) beam dynamics modeling of MEBT with realistic beam distributions from the RFQ.

2. Proton RFQ MEBT design.

The MEBT line follows the RFQ. It shapes the RFQ output beam to transfer it through the long existing common transport to the DTL with minimal losses. The new MEBT elements immediately downstream the proton RFQ are four electromagnetic (EM) quadrupole magnets and two buncher cavities [2], see in Fig. 2 (elements 1-12), which shows Trace 3-D beam envelopes from RFQ to DTL. They occupy about 0.9 m along the beam line and must have reasonably small transverse dimensions, because the two injector lines are very close to each other near the merging point. These four quads and two bunchers are followed by a 0.5-m long drift to the merging point (at element 14) to the common transport line, which continues for about 2.7 m to the DTL entrance. Important parameters for our analysis are also the transverse beam pipe sizes in the proton injector line: its inner diameter (ID) 1.875" (radius $a \approx 2.381$ cm) and outer diameter 2"; the pipe wall thickness is 1/16" (≈ 0.159 cm). As one can see from Fig. 2, the beam size in the MEBT can be rather large, approaching the beam-pipe radius. This is caused by the necessity to transport the beam after MEBT through the long common beam transport line.

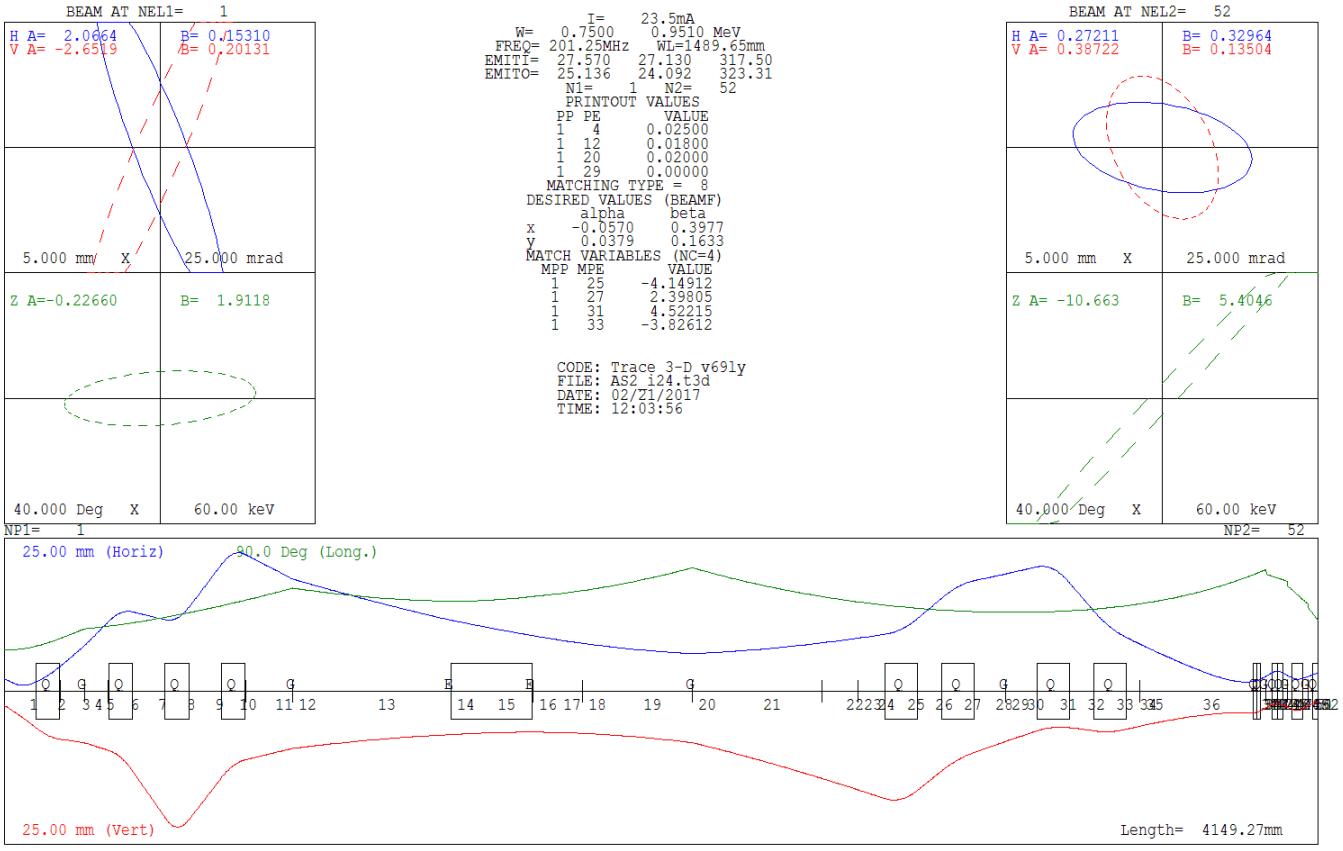

Figure 2: Trace 3-D: proton RFQ MEBT and common transport beam envelopes from RFQ to DTL.

3. MEBT elements.

The main MEBT elements – quarter-wave (QW) bunchers and EM quadrupole magnets – were analyzed in [4]. Here we provide a short summary, plus discuss the beam steering in MEBT with additional windings in the quads.

QW bunchers. A compact quarter-wave (QW) buncher cavity (λ/4-resonator) was originally proposed [5] as a potential replacement for the existing LANSCE 201.25-MHz main buncher (MB), which is a much larger re-entrant TM_{010}-mode cylindrical cavity. Using such a QW resonator as a de-buncher to improve the LANSCE operation with multiple beam species was suggested in [6]. The QW buncher is more than three times shorter (beam-line footprint) compared to the re-entrant MB, as well as more than six times smaller transversely when oriented properly. Its smaller dimensions give more options for designing the beam lines near the merging point. The QW resonator has a coaxial geometry with a central stem that supports a drift tube; when combined with additional two half-drift tubes, it forms a two-gap cavity, see Fig. 3. The gap spacing is $\beta\lambda/2 = 2.98$ cm for 750-keV protons ($\beta = 0.04$), which makes the QW cavity significantly more compact than the TM pillbox cavity.

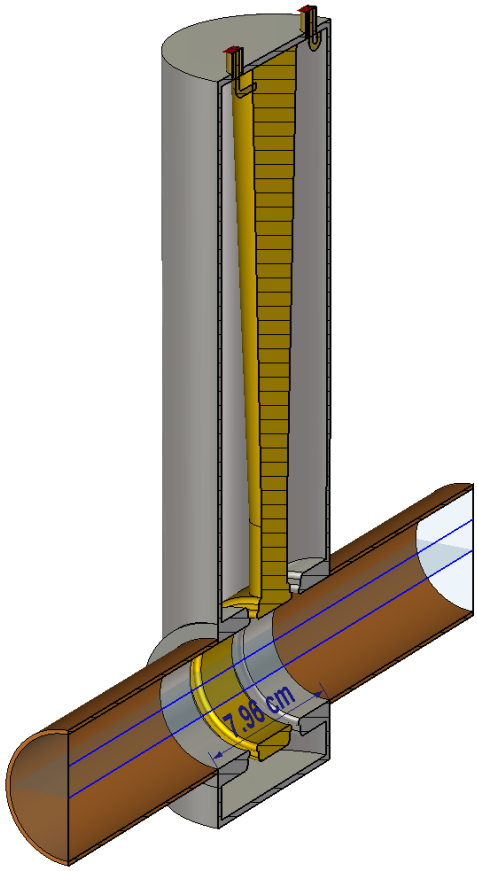

Figure 3: CST Studio model of the quarter-wave buncher cavity for the proton RFQ MEBT with beam pipes. Cut view shows RF feed, coupler loop, and field probe.

The QW buncher has a length along the beam axis of ~8 cm and height of ~29 cm. By comparison, the TM pillbox has a footprint of 28 cm in length and is 50 cm in diameter. In the proton MEBT the bunchers are also very close to quads, cf. Figs. 1-2. Therefore, the cavity aperture size should match the beam pipe size, i.e. to have radius a = 2.38125 cm. The modified QW buncher model is shown in Fig. 3.

We calculated eigenmodes of the modified buncher with CST MicroWave Studio in [4]. The adjusted geometrical parameters and cavity EM results are summarized in Table 1 (voltage-dependent parameters are in blue). The maximal effective voltage $V_{\text{eff}} = E_0TL$, where E_0 is the cavity gradient, L is its length, T is the transit-time factor, for the proton MEBT buncher is 25 kV, i.e. 12.5 KV per gap [2]. We increased this value by 20% safety margin for our analysis. In the QW cavity the power is dissipated predominantly along the central stem, 71% versus 28% on the outer cavity cover and 1% on the RF feed and field probe. It seems natural to put a water-cooling channel inside the stem.

The cavity frequency tuning can be achieved by moving (bending) the cylinder bottom surface. The tuning sensitivity in Table 1 assumes that the bottom surface moves as a whole. It will be almost the same if a thin bottom is bent (protrudes near its center), since the cavity fields are mostly concentrated near the center of the bottom surface.

Table 1. Parameters of 201.25-MHz QW buncher cavity for proton MEBT.

Parameter	**Value**	**Comment**
Beam aperture radius, cm	2.38125	Matching the beam pipe
Length along the beam axis L, cm	7.96	With two side walls of 2.5-mm thickness
Inner height of the resonator, cm	27.55	From top to bottom of the cylinder
Gap width, cm	0.8	Can be changed
Distance between the gaps, cm	2.98	$\beta\lambda/2$, fixed
Frequency tuning sensitivity df/ds, MHz/cm	-2.39	Moving the cylinder bottom surface up
Transit time factor T	0.491	
Quality factor Q *	3897	Assuming ideal copper $\sigma = 5.8 \cdot 10^7$ S/m
Loaded quality factor	3320	With 50-Ω RF coaxial feed
R/Q, Ω	110.4	
Effective shunt impedance ZT^2, MΩ/m*	1.31	
Reference effective voltage E_0TL, kV	30	15 kV per gap (design max + 20%)
Average gradient E_0, MV/m	0.767	
Total surface-loss power, W	4332	At 100% duty
Average dissipated power at 15% DF, W	650	
Maximal surface electric field, MV/m	17.4	$=1.18E_K$ (E_K=14.77 MV/m at 201.25 MHz)

* Assuming ideal copper walls with conductivity $\sigma = 5.8 \cdot 10^7$ S/m

The plots of the cavity electric field scaled to the maximal value of effective voltage per gap V_{eff} of 15 kV are shown in Fig. 4. The longitudinal components of the electric field on two axes, which are displaced by half-aperture in either x- or y-direction from the cavity axis, are practically the same and somewhat higher than on the cavity axis. The transverse electric field on the cavity axis is very small but the radial component becomes comparable to the longitudinal one on two shifted axes, and will be even larger near the aperture wall. Note that the longitudinal field is an odd function of z (z = 0 is the cavity center), while the transverse components are even functions of z.

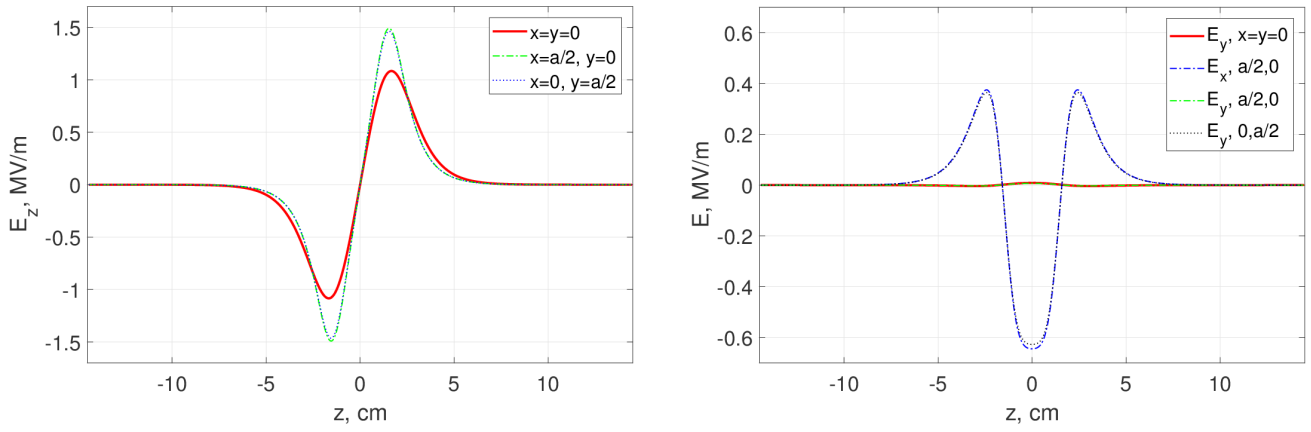

Figure 4: Longitudinal (left) and transverse (right) electric field in the MEBT QW buncher on three axes: the cavity axis (x=0, y=0) and two axes shifted by half-radius (x=a/2, y=0) and (x=0, y=a/2).

MEBT quadrupole magnets and beam steerers. Because of restricted space in the proton MEBT, we consider the compact design for electromagnetic quadrupoles that originated at the APT/LEDA, see [7]; it was further developed for the SNS project [8]. The proton MEBT magnets have a 5-cm thick solid core of low-carbon steel, which is assembled of four quadrants. The right and left halves are bolted and pinned together, so the magnet can be assembled around the beam pipe. All connections are on the outer

edges of the right and left halves. A CAD model of the MEBT quadrupole magnet with added steering coils is shown in Fig. 5. The core material for magnet field calculations with CST ElectroMagnetic Studio (EMS, [3]) was low-carbon steel 1008. Some quadrupole dimensions, design parameters, and EMS calculated values are listed below in Table 2. Compared to [4], the quad aperture was increased by 1 mm to facilitate quad mounting and alignment. The iron length was slightly reduced to keep the same effective length, but the main change is that the currents are about 8% higher for the larger aperture. Similar to [4], the quad gradient falls to 0.01 of its maximal value at about 10 cm from the quad central transverse cross section.

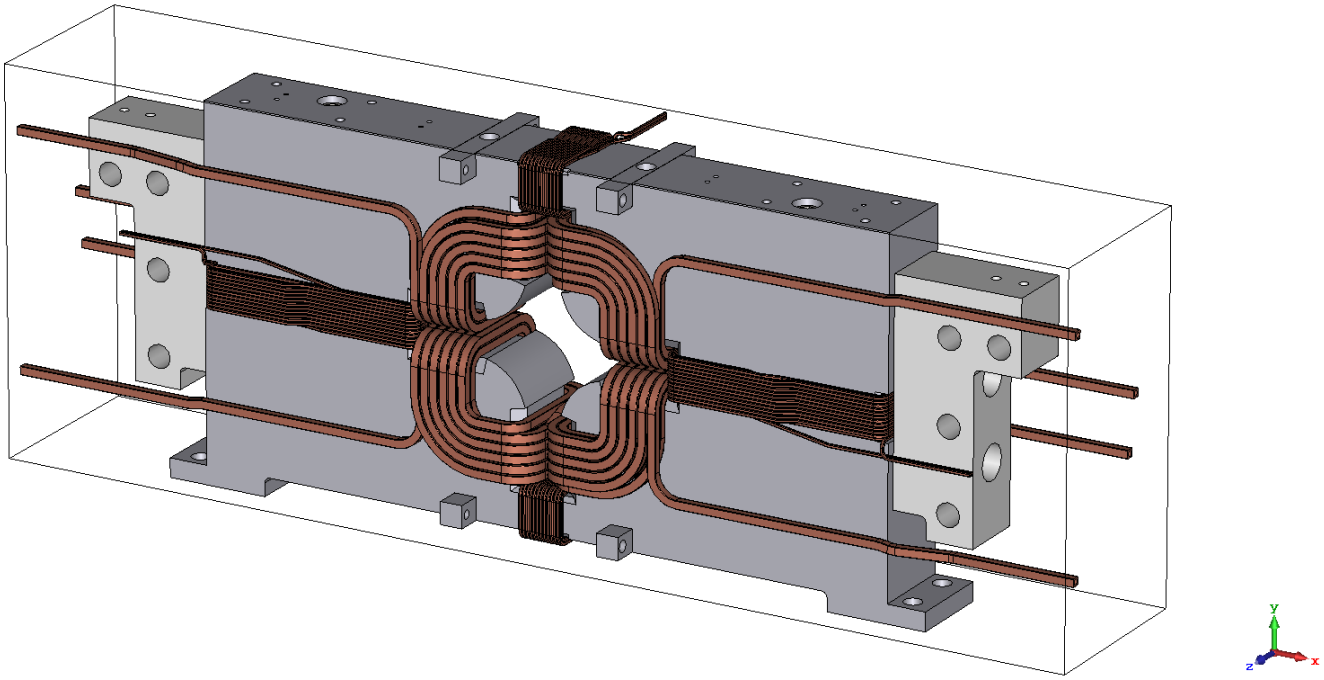

Figure 5: CAD model of MEBT quadrupole [9] imported in CST; core steel (grey) and current coils (copper): four quadrupole coils and two pairs of steerers, for horizontal (in x) and vertical (in y) steering.

Table 2. Parameters of proton MEBT quadrupoles.

Parameter	**Value**	**Comment**			
Quadrupole aperture radius a, cm	2.64	The outer beam pipe radius + 1 mm			
Iron length along the beam axis L, cm	5.018				
Iron half-width (in x), cm	12	Can be extended to facilitate access			
Iron half-height (in y), cm	10				
Effective quad length L_{eff}, cm	7.60				
Design parameters for Q1 to Q4:		Q1	Q2	Q3	Q4
Type		D	F	D	F
Gradient G, T/m		-8.3255	8.5489	-10.7794	7.1347
GL, T		-0.6327	0.6497	-0.8192	0.5422
EMS calculated values for Q1 to Q4:		Q1	Q2	Q3	Q4
effective length, cm		7.6002	7.6002	7.6002	7.6002
coil current, A·turns		2322	-2385	3007	-1990
gradient G, T/m		-8.3231	8.5491	-10.7797	7.1324
GL, T		-0.6326	0.6497	-0.8193	0.5421

Ideally, one wants only the vertical component B_y of the magnetic field for horizontal steering (in x) of the beam moving in the z direction, and only horizontal component B_x to steer the beam vertically. The simplest way to produce such fields is by using dipole magnets but the MEBT does not have space to add dipoles. In the MEBT quads, two pairs of additional windings on the same steel core provide beam steering. This is illustrated in Fig. 6, which shows magnetic field arrows produced by the horizontal steerers, and in Fig. 7, where the field components are plotted along the quad axis $x = y = 0$ and shifted axis $x = y = 1$ cm.

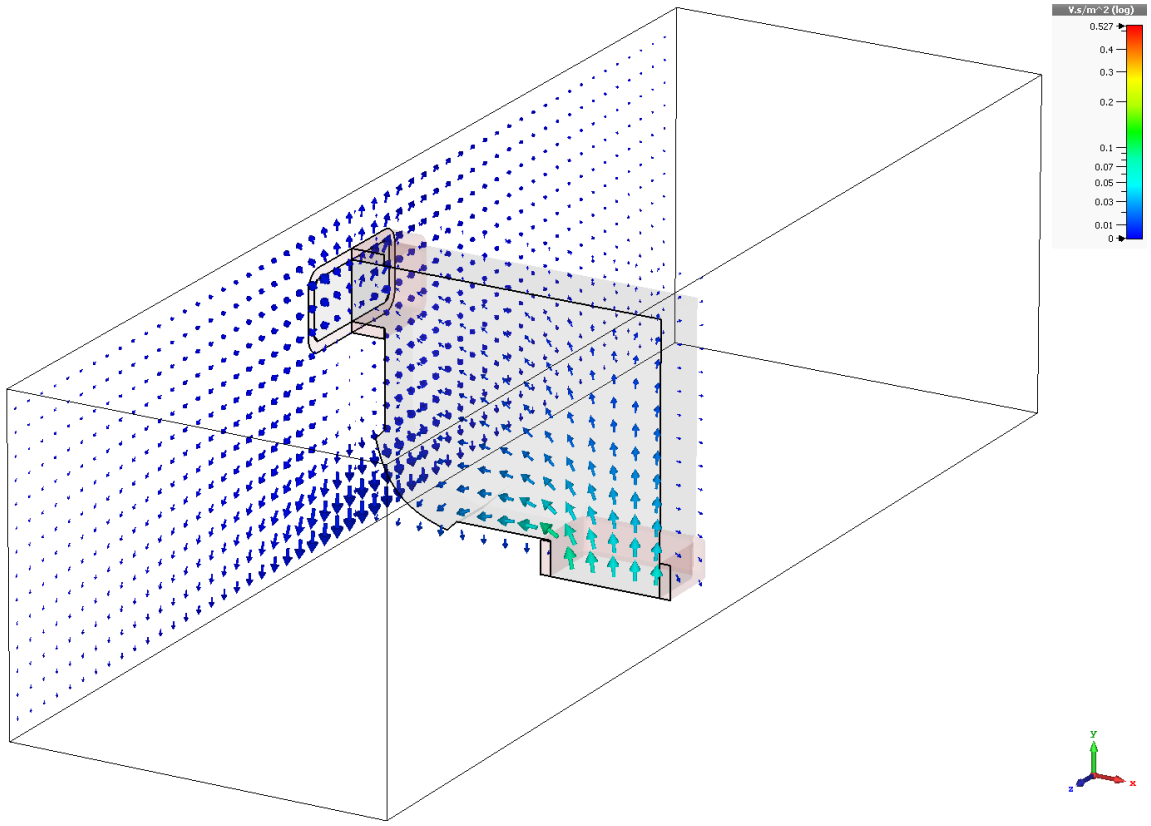

Figure 6: Magnetic field of horizontal steerers in two planes: the quad central transverse cross section $z = 0$ and the longitudinal vertical cross section $x = 0$. Only one quarter of the magnet is shown.

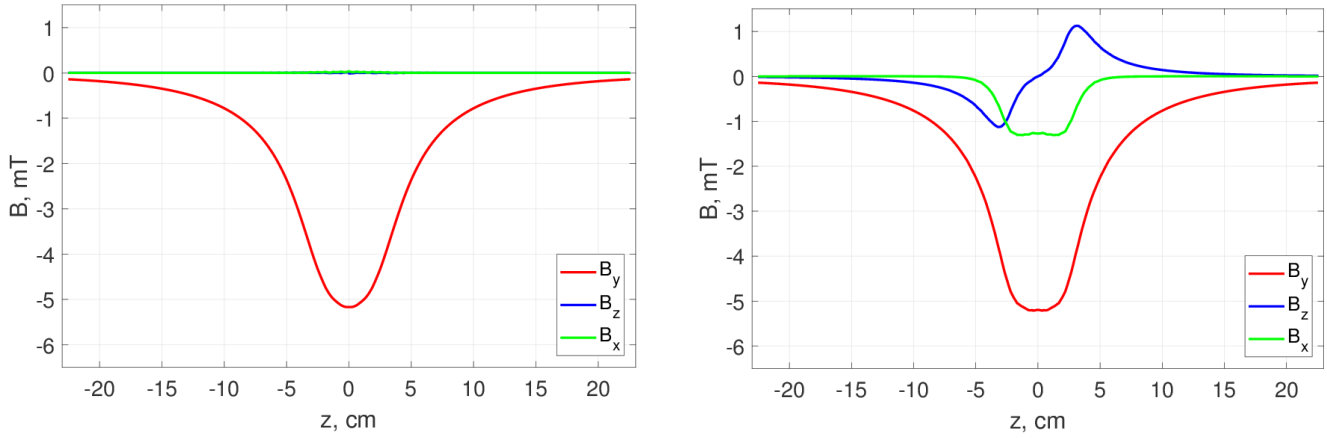

Figure 7: Magnetic field components of horizontal steerers on two axes: the quad axis $x = y = 0$ (left) and shifted axis $x = y = 1$ cm (right).

The field values in Fig. 6-7 correspond to the total current 200 A in each of the two horizontal steerer coils. Each steerer coil consists of 24 turns of copper wire. One can see from Fig. 7 (left) that the horizontal steerer field on axis has only one component, B_y, as needed. The magnetic field extends rather far from the quad. However, on the shifted axis, Fig. 7 (right), there are noticeable components B_x and B_z, so there is some x-y coupling. Off-axis particles in such a field will be deflected not only in the horizontal direction but also vertically. More quantitatively, the field integrals $I_y = \int B_y(z)dz$ and $I_x = \int B_x(z)dz$ are summarized in Table 3. The table also gives the corresponding total deflection angles for 750-keV protons ($\beta = 0.04$) passing through such a steerer.

Table 3. Steerer parameters for proton MEBT.

Parameter	**Value**	**Comment**
Horizontal deflecting field integral I_y	$-6.36\cdot10^{-4}$ T·m	On axis, $x = y = 0$
Vertical deflecting field integral I_x	$1.1\cdot10^{-6} \approx 0$ T·m	On axis
Horizontal deflecting angle	5.1 mrad	On axis
Vertical deflecting angle	≈0	On axis
Horizontal deflecting field integral I_y	$-6.34\cdot10^{-4}$ T·m	On shifted axis, $x = y = 1$ cm
Vertical deflecting field integral I_x	$-8.7\cdot10^{-5}$ T·m	On shifted axis
Horizontal deflecting angle	5.1 mrad	On shifted axis
Vertical deflecting angle	-0.7 mrad	On shifted axis

4. Beam dynamics.

Here we apply the calculated 3D fields of the MEBT elements to perform Particle Studio (PS) particle-in-cell (PIC) beam dynamics modeling of MEBT. Since the proton beam size in the MEBT is large – comparable to the beam-pipe aperture, cf. Fig. 2 – using the calculated fields is important to account for 3D field effects at large radii. For initial beam distributions in MEBT PIC modeling we use two realistic distributions for the proton beam at the RFQ exit from previous 10K macro-particle simulations of 24-mA RFQ input: one is the ParmteqM output [10], another from our PS simulations [11] with MWS-calculated RFQ fields. Some parameters of these initial beam distributions are summarized in Table 4.

Table 4. Initial beam distribution parameters for MEBT PS simulations.

Parameter	**Units**	**ParmteqM**	**PS**
Proton beam current	mA	23.5	22.6
Number of macro-particles		9788	9397
Averaged particle energy	keV	750	754
Averaged horizontal coordinate x	mm	$4.1\cdot10^{-3}$	-0.16
Averaged vertical coordinate y	mm	$4.4\cdot10^{-3}$	0.43
Averaged horizontal angle x'	mrad	$-6.9\cdot10^{-2}$	-6.7
Averaged vertical angle y'	mrad	$6.9\cdot10^{-2}$	6.2
Normalized rms horizontal emittance ε_x	π μm	0.22	0.25
Normalized rms vertical emittance ε_y	π μm	0.22	0.25
Rms longitudinal emittance ε_z	π μm	0.28	0.35
Maximal time spread, max(t)-min(t)	ns	1.23	0.97
Rms time spread σ_t	ns	0.15	0.14

One should add that these two distributions were recorded at two different locations: the ParmteqM output was recorded at the exit inner RF wall of the RFQ box, while the PS results were recorded in the RFQ exit beam pipe, in the transverse plane 4.5 cm downstream of the RF inner wall. We start our PIC simulations at $z_0 = 0$, but make two CST PS models of different lengths, $z_{max} = 106.17$ cm or 101.67 cm. In both cases, the PIC simulations end at 15 cm downstream the center of the second buncher cavity, in the field-free region.

The following steps include making a cylindrical vacuum beam pipe and importing properly scaled buncher RF fields and magnet fields in the corresponding locations of the model. The quad magnetic fields correspond to the design values [2], see also in Table 2. For the first buncher (B1) we scale to the maximal effective total voltage of $V_1 = 25$ kV (12.5 kV per gap for the 2-gap buncher), for the second (B2) to $V_2 = 18$ kV. The correct choice of RF phase for a buncher cavity means that the bunch head (particles ahead of the synchronous one) are slowed down while the tail particles are accelerated; the synchronous particle does not change its energy. For protons in a 1-gap buncher this means that the RF phase should be -90° when the bunch center is at the gap center. Small deviations from this value can be used to correct the bunch energy. In 2-gap bunchers, the gaps are spaced by $\beta\lambda/2$, or by 180°. For the longitudinal electric field profile shown in Fig. 4 (left) – first a "dimple" then a "bulge" at 0° RF phase – the proton bunch center should arrive at the cavity center (the middle between gaps) at 180°. Obviously, for both bunchers the bunch length should be less than $\beta\lambda/2$ to avoid bunch breaking.

The beam dynamics in the MEBT is modeled with the CST PS Particle-in-Cell (PIC) solver. For the initial PS runs, no steering was applied. The particle parameters were recorded at different locations along the MEBT using 2-D plane particle monitors as shown in Fig. 8. The monitor plane locations are at the first quad center (Q1), three planes near buncher 1 (B1-5cm, B1, B1+5cm), centers of quads Q2, Q3, Q4, three planes near buncher 2 (B2-5cm, B2, B2+5cm), and the PS simulations exit plane at B2+15cm.

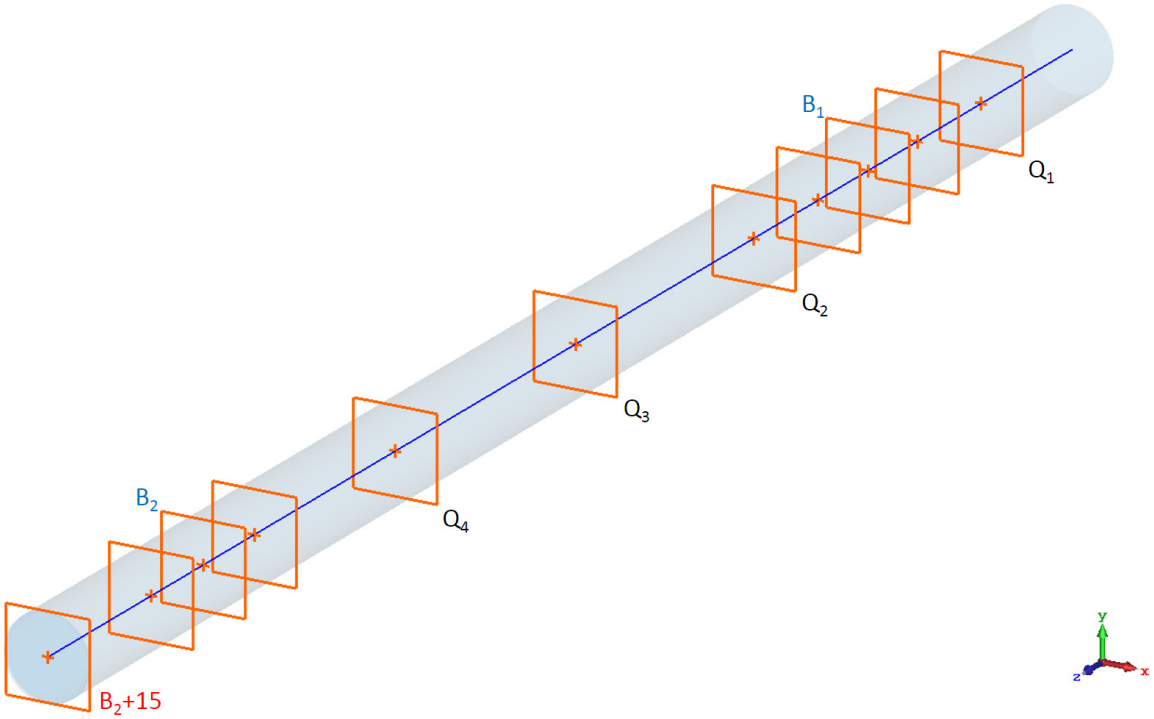

Figure 8: Locations of 2-D plane particle monitors along the MEBT. The beam travels from right to left.

When the initial beam distribution was prepared for PS, we adjusted the particle initial time delay so that the bunch center arrives at the center of buncher 1 (B1) at 0° RF phase. Then the RF phase of B1 is set to 180°, and for B2 it is adjusted to have the correct bunching (152°). This is for the case of the initial ParmteqM distribution. For the PS input beam, the beam energy correction is needed, so the RF phases are 167° in B1 and 152° in B2.

The positions of the beam transverse center and averaged angles found by post-processing the monitor records are shown in Fig. 9. The two top plots are for the ParmteqM input initial distribution, and two bottom ones are for the distribution that was produced by the PS simulations of the RFQ. The plot-point locations are, correspondingly, the input plane (z = 0), the first quad (Q1), three points near buncher 1 (B1-5cm, B1, B1+5cm), quads Q2, Q3, Q4, three points near buncher 2 (B2-5cm, B2, B2+5cm), and the simulations exit plane at B2+15cm.

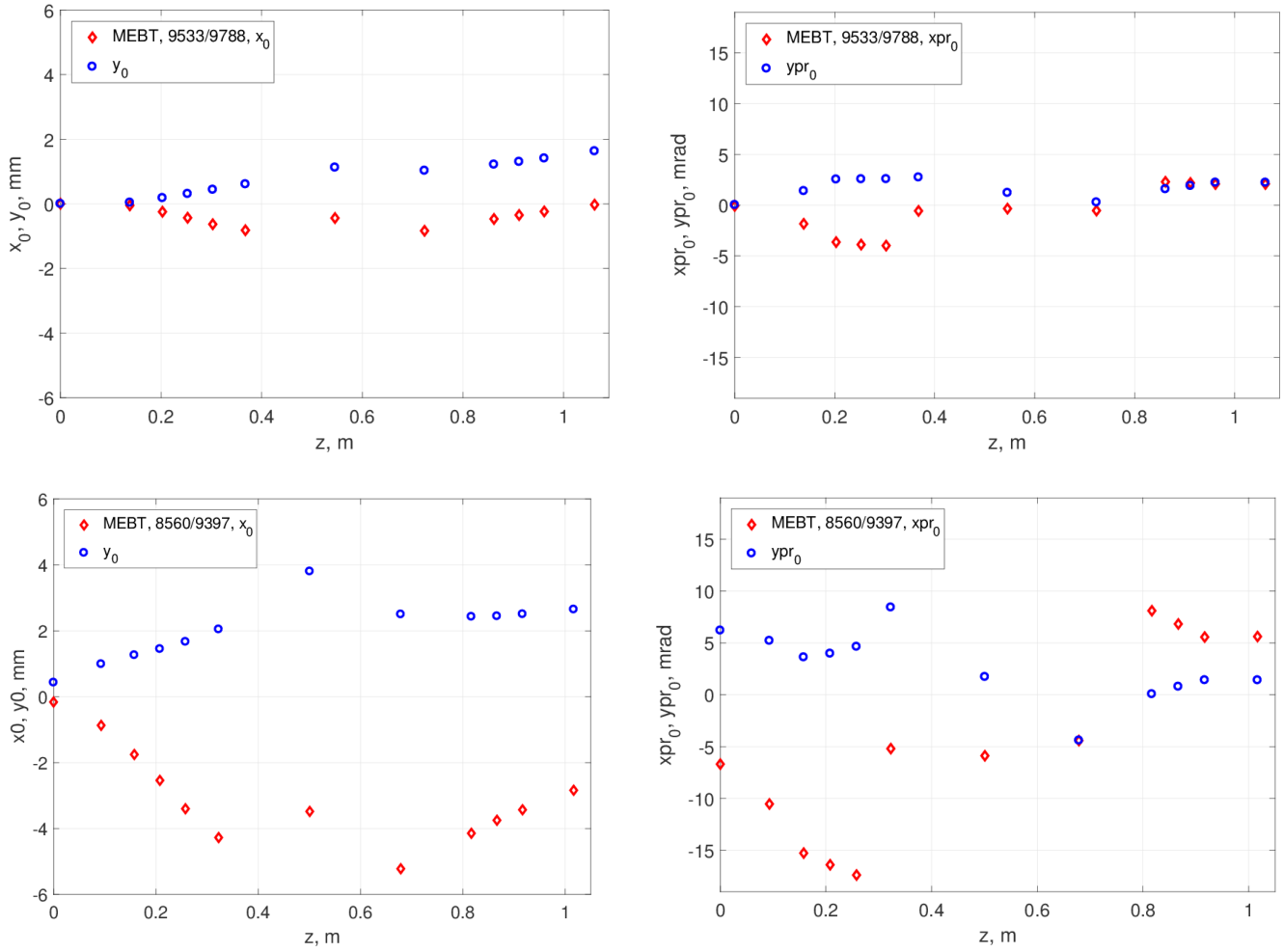

Figure 9: The beam average transverse position (left) and angle (right) for x (red) and y (blue) along the MEBT for two input distributions, from ParmteqM (top plots) and PS (bottom ones).

One can see that even for the well-behaved ParmteqM initial distribution, the beam center is slightly off axis (within 2 mm). The PS distribution already has some noticeable initial average angles, and the off-axis deviations can be as large as 5 mm, with tilt angles more than 15 mrad without steering.

Particle losses are indicated on the plots (N_{out}/N_{in}) in Fig. 9, and they are significant in the PS-input case, 9%, compared to 2.6% for the ParmteqM input. The plot of $N(t)$ for the PS input in Fig. 10 (top) shows where the losses occur. The initial step up shows the injected bunch, while the step down corresponds to the exiting bunch. The particles are lost mostly between Q2 and Q4. In fact, in PS runs one can see directly on screen how the particles are scraped by the chamber wall as the beam size increases after B1 and the beam is steered off axis by the quad fields. Obviously, some beam steering in MEBT is needed.

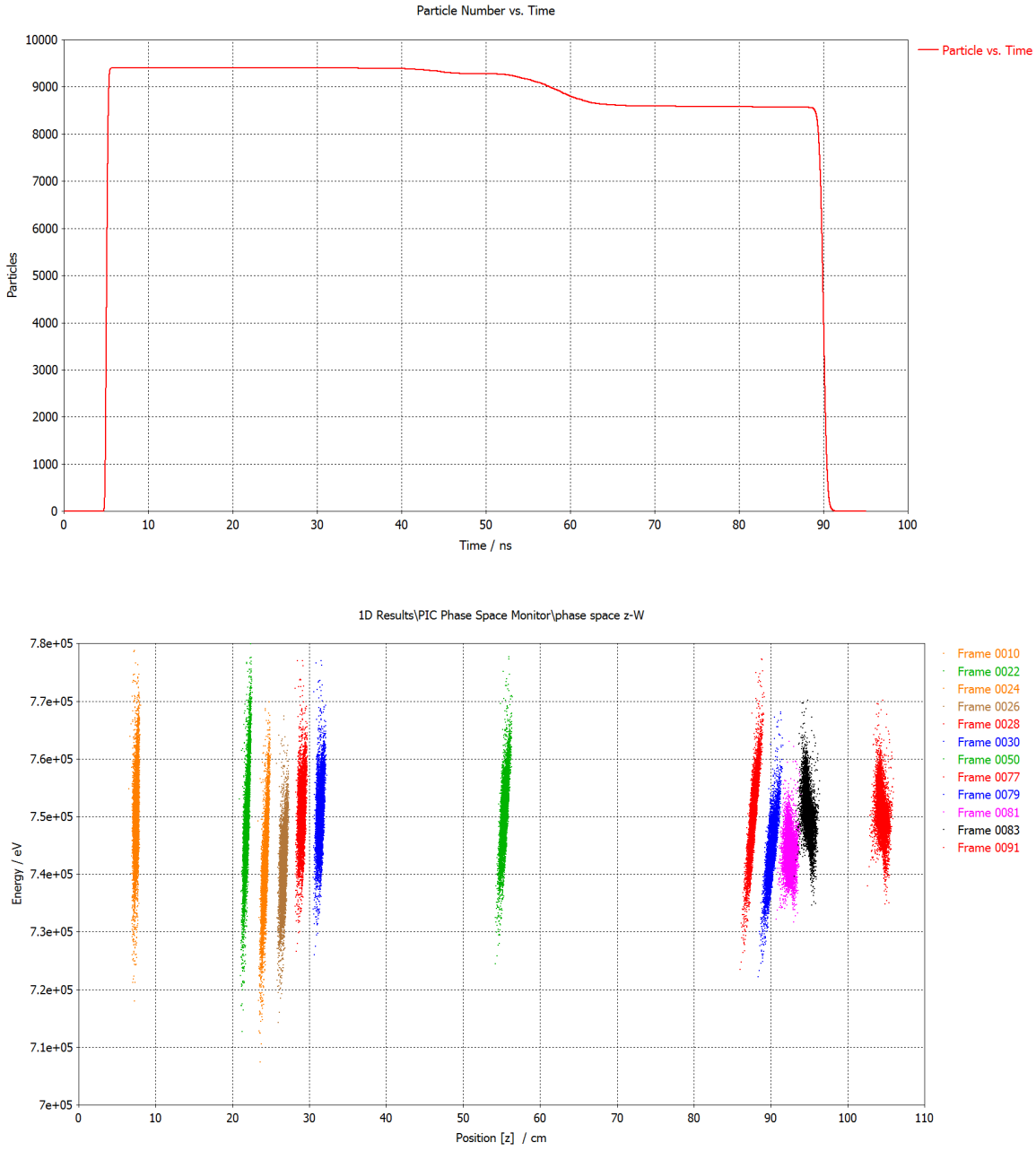

Figure 10: The number of macro-particles versus time in PIC simulations with PS input distribution (top) and snapshots of the longitudinal phase space with ParmteqM input distribution (bottom).

There are various steering choices; the simplest one is to minimize the beam-center displacements along the MEBT. The steering is easy for the ParmteqM input: with all steering currents below the value of 200 A used for reference in Sec. 3, one can keep all displacements within a fraction of 1mm and all tilts

below 1 mrad. For the PS input beam, which has initial significant tilt angles, steering currents up to 4.7 times the 200 A are required to keep the deviations below 1 mm. With the beam steering implemented, the particle losses are reduced: slightly for ParmteqM input – from 2.6% to 2.1%, but significantly for PS input – from 9% down to 3.2%.

The evolution of the longitudinal phase space in MEBT is shown in Fig. 10 (bottom) for the case of a steered ParmteqM beam. The selected snapshots show the beam shortly after injection (Frame 10, $t = 10$ ns), with a wide energy spread and forward tilt (higher energy particles are in the bunch head); passing through B1 (Frames 12-30); in the middle of MEBT (Frame 50); through B2 (Frames 77-83); and near the MEBT exit (Frame 91). Note that the bunch tilt near the exit is backward (higher energy particles are behind) and the energy spread is reduced. Therefore, the faster particles will catch up with the slower ones during the bunch transport to DTL and the bunch will be effectively compressed longitudinally.

However, the beam transverse emittances increase significantly even for the steered beams, as illustrated by plots in Fig. 11, where the evolution of the normalized rms transverse emittances and the longitudinal rms emittance along the MEBT is shown. One can see that the horizontal emittance ε_x increases by about a factor of 3 even for the ParmteqM input distribution, while the vertical emittance ε_y grows by a factor of 2. The horizontal emittance jump occurs after the quad Q3, while the vertical one starts to increase after Q2. The longitudinal emittance also increases, but not as much, by about 30% for both distributions, mainly in the second buncher, B2.

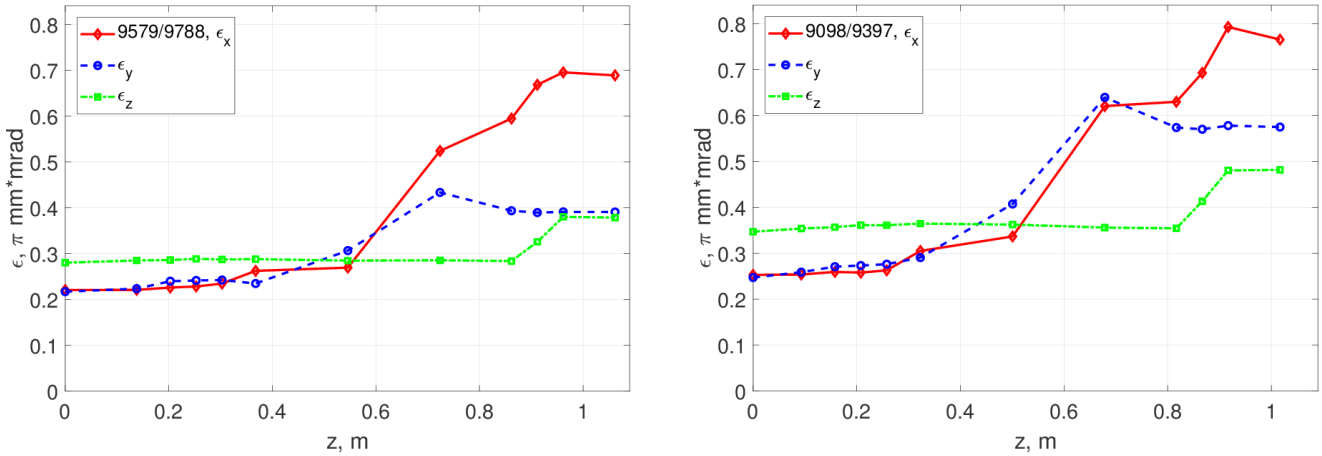

Figure 11: Emittance growth along the MEBT for the ParmteqM input (left) and PS one (right).

Such large values of the transverse emittances after the MEBT are unexpected and significantly higher than the predictions of the envelope codes and Parmila modeling used in the MEBT design [2]. We need to find out the reasons for this large emittance growth and how it can be mitigated. To do that, we look at the physical differences in the Trace / Parmila model and the CST model of the MEBT. First, the Parmila simulations use hard-edge perfect quadrupole fields: $B_x = Gy$, $B_y = Gx$, and $B_z = 0$, where G is the quad gradient, within the quad effective length; outside that region the fields are set to zero. Second, the buncher RF fields in Parmila are represented as zero-length single gaps, with longitudinal and transverse kicks to the passing particles that depend on the particle radial position. Using the ParmteqM input case, we explore various MEBT configurations, e.g., by substituting the CST-computed quad fields by ideal hard-end quadrupole fields generated with a Matlab script. The results are summarized in Table 5.

Table 5: Exit beam parameters for various MEBT configurations with ParmteqM input distribution.

Case	B1	B2	Q	S	N	ε_x	ε_y	ε_z
0	initial beam parameters (cf. Table 4)				9788	0.22	0.22	0.28
1	on	on	EM	on	9579	0.69	0.39	0.38
2	on	on	HE	off	9702	0.37	0.25	0.33
3	off	off	HE	off	9783	0.27	0.25	0.28
4	off	off	EM	off	9743	0.49	0.33	0.28
5	off	off	EM	on	9747	0.44	0.34	0.28
6	1g, on	1g, on	HE	off	9650	0.42	0.26	0.36

The notations in Table 5 are as follows: S stands for steerers; N is the number of macro-particles; and the emittance units are π mm·mrad (= π μm). For quadrupoles (Q), "EM" means the EMS-calculated fields (Sec. 3) and "HE" stands for hard-edge perfect quadrupole fields. For bunchers, "on" means the effective voltage 25 kV in B1 and 18 kV in B2, with properly adjusted RF phases. In the special case 6 ("1g, on"), we used the MWS-calculated RF fields of the standard single-gap re-entrant RF buncher cavity instead of the 2-gap QW buncher fields, see in Sec. 3 and [5, 6], with the same effective voltages and proper RF phases. In practice, such axisymmetric RF cavities are too large to be placed in MEBT but we use their fields in PIC simulations for comparison with QW bunchers.

The particular cases in Table 5 correspond to the following MEBT configurations:

- Case 1: the realistic configuration with CST-calculated RF and magnetic fields. It is the case discussed above and illustrated in Fig. 11 (left), characterized by significant emittance growth.
- Case 2: similar to case1 but the real quadrupole fields are replaced by ideal hard-edge (HE) ones. The beam steering is practically not needed in this case. The emittance increase is strongly reduced compared to case 1.
- Case 3: RF buncher fields are turned off (no bunchers), ideal quadrupole focusing, steering is not needed – essentially the RFQ beam is just transferred through quads. This is a reference case that provides minimal emittance growth. Of course, in this configuration the beam after MEBT does not have the required properties and will not be properly transferred through the following common beam line and injected into the DTL (the same is also true for cases 4 and 5).
- Case 4: similar to case 3 (no bunchers) but with realistic quad fields. The transverse emittance growth is higher than in case 3 but lower than in case 1.
- Case 5: similar to case 4 but with steering. The comparison of cases 4 and 5, both with bunchers off and realistic quadrupoles, shows that the steerer effect is small but positive.
- Case 6: QW buncher RF fields are replaced by equivalent CST-calculated RF fields of reentrant 1-gap bunchers. From comparison of cases 2 and 6, the QW bunchers work slightly better than re-entrant bunchers with the same aperture.

For further discussion of the results, it is more convenient to consider relative changes of the beam parameters in the MEBT, which are summarized in Table 6. First, we notice that the transverse emittances increase due to only space charge effects by about 15-20%, cf. case 3. The buncher fields mostly affect the horizontal emittance as can be concluded from comparison of cases 2 and 3, increasing it by a factor of 1.5 on top of the space charge increase. When the bunchers are off, the realistic quad field increase the horizontal emittance by approximately a factor of 1.75 above the space charge, cf. cases 3, 4, and 5. The combined effect of the buncher RF fields and the realistic quadrupole magnetic fields on the transverse emittances is approximately multiplicative.

Table 6: Relative parameter changes for various MEBT configurations with ParmteqM input.

Case	B1	B2	Q	S	N_{out} / N_{in}	ε_x / $\varepsilon_{x,in}$	ε_y / $\varepsilon_{y,in}$	ε_z / $\varepsilon_{z,in}$
0	initial beam parameters (cf. Table 4)				1	1	1	1
1	on	on	EM	on	0.979	3.14	1.77	1.36
2	on	on	HE	off	0.991	1.68	1.14	1.18
3	off	off	HE	off	0.999	1.23	1.14	1
4	off	off	EM	off	0.995	2.23	1.50	1
5	off	off	EM	on	0.996	2.0	1.55	1
6	1g, on	1g, on	HE	off	0.986	1.91	1.18	1.29

One can conclude that some modifications of the MEBT are necessary, since the transverse emittance increase in the present configuration is too high. The first step would be to modify the quadrupole design to reduce the magnetic field non-linearities at large radii and edge fields, which are the largest contributors to the emittance growth. If the resulting emittance decrease is insufficient, the changes in the MEBT design should be considered.

We conclude this Section with a few comments on computational details of the MEBT PIC simulations. Most of the runs in Tables 5-6 were performed using PS hexahedral meshes of 4-8 M mesh points. A typical run with 10K particles on a 4M mesh takes about 35 minutes on a 40-core PC with Nvidia Quadro K6000 GPU or 2.75 hours on a 16-core PC without GPU. However, the PS results are not very different for rougher meshes with approximately 0.6M mesh points, which take only ~15 min, either with or without GPU; such meshes were used for tuning beam steering. The main difference is that final emittances are slightly higher with finer meshes, on the level of a few percent. The results recorded by PS 2-D particle monitors, cf. Fig. 8, are post-processed in Matlab.

5. Possible modifications of MEBT elements.

There are a few options to improve the MEBT performance. They range from relatively simple modifications of quadrupoles to a complete MEBT redesign. Probably, we do not have much freedom with changing RF bunchers: as was noted above, standard re-entrant cavities, even if they were possible in a compact MEBT, do not reduce the emittance growth. On the other hand, the MEBT quadrupoles, which are the largest source of the emittance problems, can be modified in various ways. One option is to increase the quad aperture, so that the beam passes through more linear part of their magnetic field. The price to pay is higher coil currents, which can be offset somewhat by increasing the core length along the beam. In addition, opening the quad aperture leads to expanding its field region further from the magnet.

A more attractive option is to extend the inner part (radially inside the coils) of the steel core along the beam pipe without changing coils. This approach will not even increase the quad footprint on the beamline if the extension does not protrude outside the coils. The modification can be achieved by making an assembled core in each quadrant, as shown in Fig. 12 (left); compare with Fig. 5. Of course, this change can be done with or without the aperture increase: it increases the quadrupole effective length and the length of the good-quality quadrupole field. When the aperture is unchanged, lower currents are needed to keep the same product GL.

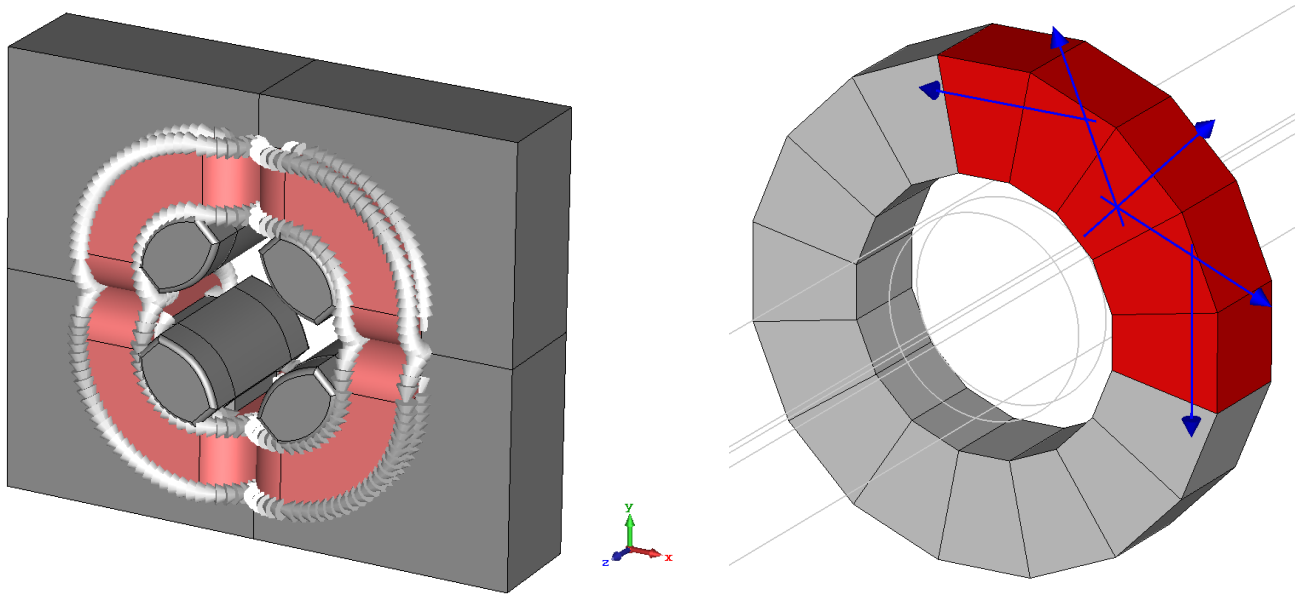

Figure 12: CST models of: (left) EM quadrupole with inner core extensions: steel (grey) and current coils (red); (right) 16-segment permanent-magnet quadrupole (PMQ): blue arrows show direction of segment magnetization (due to symmetry, one-quarter geometry is sufficient for field computation).

Another simple option is replacing the EM quadrupoles with permanent-magnet quadrupoles (PMQs). A CST model of 16-segment PMQ is shown in Fig. 12 (right); the inner and outer cylindrical collars that keep the PM blocks together are not shown. With the magnet length 2 cm, inner radius 2.75 cm, outer radius 5 cm, and a typical PM material (e.g., SmCo) with the remnant field $B_0 = 1$ T, this PMQ provides approximately the required value of the product GL, see in Table 2. Note that the PMQ is shorter and more compact than the EM quad in Fig. 4. Its gradient is higher but the effective length is smaller, about 3 cm. Making 4 PMQ with slightly different GL can be achieved by either small adjustments of PMQ geometry or by using 4 identical PMQs (cheaper!) with outer magnetic shields that have properly adjusted dimensions. The external steel shield clamps the PMQ magnetic field and prevents overlaps with adjacent elements. Obviously, PMQs do not allow easy focusing adjustments that can be done by changing currents in EM quads. Another PMQ disadvantage is that separate steering magnets are needed for beam steering.

One more option is to change the transverse cross-section profile for the EM quad pole tips to improve the field quality. The profile for the pole tips in EM quads of Fig. 4 is a standard hyperbola $x \cdot y = a^2/2$ truncated at the polar angle 14° from axis at both edges. By adjusting the profile, one can reduce the effects of the edge fields in the integrated product GL at large radii. One particular modification of the pole shape was considered [12]; we will call this configuration "alternative" EM quads. The pole shape modification can be combined with the quad core extensions discussed above.

The results of PIC simulations with PS input distribution are compared for standard EM quadrupoles and two types of their modifications in Table 7, which is similar to Table 5 but has another input beam. The case "p0" is the initial PS beam distribution with parameters listed in Table 4. The case "p1" corresponds to the results of PIC simulations with the standard EM quads discussed above and shown in Fig. 11 (right). In the case "p2" the EM quads are replaced by ideal hard-edge quads, plus "ideal" hard-edge steering (pure B_x and/or B_y) is used in quads 1 and 4; essentially, this configuration gives only the buncher field effects. In the case "p3" the EM quads fields are replaced by those of PMQs that have the

design values of *GL* from Table 4. Finally, for the case "p4" the standard EM quad fields are substituted by those of quads with "alternative" pole shape.

Table 7: Exit beam parameters for various MEBT configurations with PS input distribution.

Case	B1	B2	Q	S	N	ε_x	ε_y	ε_z
p0	initial beam parameters (cf. Table 4)				9397	0.25	0.25	0.35
p1	on	on	EM	on	9098	0.77	0.58	0.48
p2	on	on	HE	on, HE	9195	0.48	0.31	0.44
p3	on	on	PMQ	on	9239	0.64	0.58	0.45
p4	on	on	Alt EM	on	9123	0.74	0.57	0.48

We can see that replacing real quad fields (p1) by ideal (p2) significantly improves the MEBT output beam parameters. One can also notice that "alternative" quads give only slight improvement (p4 vs p1), but with PMQs (p3 vs p1) the improvement is more noticeable.

For the relative parameter changes, we rewrite these results in Table 8, which can be compared to Table 6 above for the ParmteqM input.

Table 8: Relative parameter changes for various MEBT configurations with PS input distribution.

Case	B1	B2	Q	S	N_{out} / N_{in}	ε_x / $\varepsilon_{x,in}$	ε_y / $\varepsilon_{y,in}$	ε_z / $\varepsilon_{z,in}$
p0	initial beam parameters (cf. Table 4)				1	1	1	1
p1	on	on	EM	on	0.968	3.08	2.32	1.37
p2	on	on	HE	on, HE	0.979	1.92	1.24	1.26
p3	on	on	PMQ	on	0.983	2.56	2.32	1.29
p4	on	on	Alt EM	on	0.971	2.96	2.28	1.37

From comparison of cases p1 in Table 8 and 1 in Table 6, one can see that the MEBT design configuration [2] influences both initial distributions in approximately the same way, except that the relative vertical transverse emittance increases slightly more for the PS input. Comparing cases p2 in Table 8 and 2 in Table 6, we can conclude that the RF buncher fields affect the PS input distribution stronger than that from ParmteqM.

Likely the MEBT design with PMQs can be further optimized to achieve improvements. In addition, one can combine PMQs and usual EM quadrupoles with steerers – for example, using two quads of each type – to improve MEBT performance. Additional studies are needed for MEBT optimization.

6. Conclusions.

We explored the beam dynamics in the MEBT for the new proton RFQ-based injector at LANSCE with CST Particle Studio particle-in-cell (PIC) 3D simulations to take into account effects of the large beam size and field overlaps. The CST-calculated fields of quarter-wave RF buncher cavities and quadrupole magnets with steerers were applied. Two realistic initial beam distributions were used in our PIC runs. We found that for both distributions the beam transverse emittances increase significantly more than was predicted in the original MEBT design [2], which was based on the standard approach using envelope codes and Parmila simulations. Our explanation for this discrepancy is that for the very large beam size in MEBT, which is required to further transfer the beam through a long transfer line to DTL, 3D field effects and field overlaps from adjacent elements become essential; they cannot be taken into

account by only traditional beam dynamics codes. From this viewpoint, the RFQ MEBT is an important example where standard simulations are insufficient to correctly predict the beam dynamics.

The emittance growth is caused mainly by the magnetic fields of short EM quadrupoles. The buncher RF fields also contribute. We considered some possible modifications of the MEBT quads and showed that they help; in particular, using permanent-magnet quadrupoles improves the MEBT performance. However, further optimization is required.

We should check (e.g., by following up with Parmila runs) how the CST-calculated MEBT output beam is transported to the DTL. If modifications of MEBT elements are not enough to reduce the emittances to acceptable values, the last resort is the most radical approach – a complete MEBT redesign. Of course, the solutions would be much easier if we could eliminate the long common transfer line between the RFQ-based injector and DTL. However, at the moment this change is not practical.

7. References.

1. R.W. Garnett et al., "Status of the LANSCE Front-End Upgrade," Proceed. NA-PAC13, Pasadena, CA (2013) 327.
2. C.M. Fortgang et al., "A Specialized MEBT Design for the LANSCE H^+ RFQ Upgrade Project," Proceed. NA-PAC13, Pasadena, CA (2013) 670.
3. CST Studio Suite, CST. www.cst.com
4. S.S. Kurennoy, "EM analysis of MEBT elements for the proton RFQ transfer line," Tech note AOT-AE: 17-009 (TN), Los Alamos, 2017.
5. S. Kurennoy, "A quarter-wave buncher cavity for the new front end of the LANSCE linac," Tech note AOT-ABS: 08-001 (TN), Los Alamos, 2008.
6. L. Rybarcyk, S. Kurennoy. "Use of a De-Buncher Cavity for Improving Multi-Beam Operations at LANSCE," Proceed. PAC09, Vancouver, BC, Canada (2009) 4944.
7. D. Barlow, LANSCE-1 tech notes TNM-98-263, -99-052, -99-072, LANL, Los Alamos, 1998-1999.
8. D. Oshatz. "MEBT Quadrupole Magnet Design Package." LBNL Eng. Note FE3312-M7861B, Berkeley, 2000.
9. J. Montross, Private communication, Aug. 2017.
10. L. Rybarcyk, Private communication, July 2017.
11. S. Kurennoy. "EM and Beam-Dynamics Modeling of the New LANL RFQ with CST Studio," report LA-UR-13-28693, Los Alamos (2013); also in "3D Effects in RFQ Accelerators," Proceed. LINAC14, Geneva, Switzerland (2014) 1077.
12. D. Shchegolkov, Private communication, Nov. 2017.